Reactant-Induced Dynamics of Lithium Imide Surfaces during the Ammonia Decomposition Process

Manyi Yang[1], Umberto Raucci[1] and Michele Parrinello[1*]

[1]Italian Institute of Technology, Via E. Melen 83, Genoa, 16152, Italy.

*Corresponding author(s). E-mail(s): michele.parrinello@iit.it;

Ammonia decomposition on lithium imide surfaces has been intensively investigated owing to its potential role in a sustainable hydrogen-based economy. Through advanced molecular dynamics simulations of *ab initio* accuracy, we show that the surface structure of the catalyst changes upon exposure to the reactants, and a new dynamic state is activated. It is this highly fluctuating state that is responsible for catalysis and not a well defined static catalytic center. In this activated environment, a series of reactions that eventually leads to the release of N_2 and H_2 molecules become possible. Once the flow of reagent is terminated the imide surface returns to its pristine state. We suggest that by properly engineering this dynamic interfacial state one can design improved catalytic systems.

Introduction

The transition to a sustainable economy passes necessarily through the development of efficient catalytic processes[1, 2]. In addition, for a catalyst to have a practical impact it should be scalable, operate at high temperature to increase yield, and still be stable in spite of these demanding requirements[3]. It is hard to imagine how in such conditions the standard model that relates catalytic activity to static structures could be applied. Since a while, it has been suggested that dynamics plays an important role in catalysis [4, 5]. However, the evidence used to support this hypothesis has been so far unconvincing since most of it is based on a series of static calculations on rather small catalytic clusters [6, 7] or on relatively short, even if highly illuminating, *ab-initio* molecular dynamics simulations[8]. Furthermore, it is not clear how dynamics could explain the high temperature stability of industrial catalysts. Additionally, the extreme *operando* conditions required by industrial processes have limited experimental investigations, that have been so far mostly restricted to studying temperatures and pressures considerably lower than those encountered in an industrial setting.

Here, we unravel the complex dynamic behaviour of a catalytic process *in operando* conditions by investigating the ammonia decomposition on a lithium imide (Li_2NH) surface, a process that has received much attention for its possible role in a future sustainable hydrogen-based economy[9, 10, 11, 12, 13, 14] We perform state of the art simulations in which the interatomic forces are calculated with an accuracy close to that of *ab initio* molecular dynamics[15]. Our simulations reveal that the reactive process induces a change of state of the interface. Such a modified interfacial state is the actual catalytic medium, and one does not need to invoke any special stable arrangement of atoms. The large fluctuations observed in the top layers of the surfaces allow a series of reactions to take place resulting in the final release of N_2 and H_2 molecules. Once the flux of reactants is stopped the catalyst reverts to its initial conditions.

Results

Reactant-induced dynamics of the surface

As a catalyst Li_2NH[16] is rather unusual since it is an ionic compound. In fact, its structural arrangement is dominated by the need to alternate divalent NH^{2-} anions and monovalent Li^+ cations (Fig. 1**a**) in order to establish local charge neutrality. The experimentally reported defective antifluorite structure does reflect this building principle[17, 18, 19]. Like many other ionic systems[20] in which there is a large difference between anionic and cationic radii, lithium imide exhibits a superionic behaviour[21, 22] with the Li^+ cations fast diffusing and the divalent imide anions oscillating around their equilibrium positions (Fig. 1**b**). As the temperature increases, Li^+ cations sitting in a tetrahedral site can move first to an octahedral empty site, and then to a tetrahedral vacancy (Supplementary Video 1 and Supplementary Figure 1). The ease with
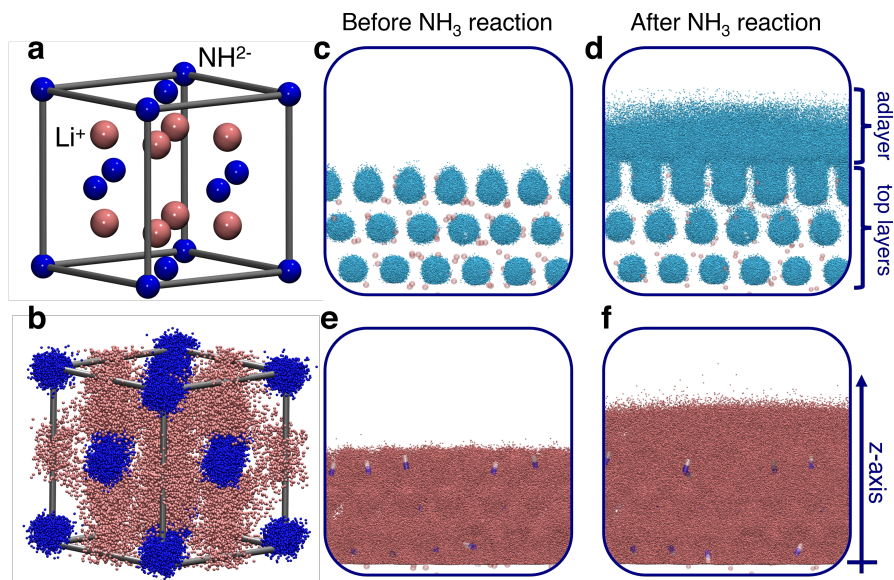
Fig. 1 Bulk and surface structure of Li$_2$NH. (**a**) Antifluorite structure of Li$_2$NH. The sublattice of NH^{2-} divalent anions is face centered cubic (FCC) whereas the Li$^+$ cations occupy the tetrahedral sites. Hydrogen atoms are omitted for clarity in panel (**a**) and in the following panels (**b-d**). (**b**) Scatter plot of N and Li atoms positions in one of the primitive cells of the simulated Li$_2$NH crystal at 600 K. Configurations are reported every 1.6 ps during a 5 ns long trajectory. Scatter plots of N (**c-d**) and Li (**e-f**) atoms positions during 0.8 μs long unbiased trajectories at $T = 750$ K before (**c,e**) and after (**d,f**) the reaction with ammonia. In panels (**c-d**) and (**e-f**) we report a configuration every 1 and 10 ps, respectively. The nitrogen atoms of the three top layers are plotted in panel (**c**), while the adlayer resulting from the ammonia reaction with the surface is also shown in panel (**d**). In panels (**e**) and (**f**) we plot only lithium atoms that have a value of the z coordinate higher than the one marked in panel (**f**). This corresponds to choosing Li$^+$ cations that are either in the top three layers and/or in the adlayer. To simplify reading, a single instantaneous configuration is chosen to represent N and H atoms. Li, N and H atoms are coloured pink, blue, and white, respectively.

which octahedral lithium interstitials can be formed facilitates the transition to the superionic state.

In order to simulate the catalytic process, one needs to perform molecular dynamics simulations in which the interatomic forces are computed from accurate electronic structure calculations so as to properly describe the forming and breaking of chemical bonds [15]. Unfortunately, such an endeavour is still computationally too expensive. However, following the pioneering work of Behler and Parrinello[23] we constructed an *ab initio* quality reactive force field by training a feed-forward neural network[24] to reproduce total energies and forces computed using density functional theory[25] (DFT), and in particular we use here the PBE exchange and correlation functional[26].

The training configurations were chosen using an active learning approach similar to that of Ref. 27, 28, 29. A detailed description of the procedure

adopted can be found in the Methods Section. During both training and simulation, we used enhanced sampling methods[30] to generate reactive events in an affordable computational time. This approach is very general and, if applied carefully, can be successfully used to study complex processes ranging from nucleation[31,27] to phase transition[29,32] and chemical reactivity in complex environments[28,33]. Following this workflow we trained a potential able to describe the Li_2NH superionic behaviour (see Supplementary Figure 2), the properties of Li_2NH surfaces, its interactions with ammonia, and the subsequent reactions leading to NH_3 decomposition into N_2 and H_2.

Since it is not known which surface is the most active, we have taken a conservative approach and chosen to study the (111) cleavage surface at the *operando* temperature of $T = 750$ K. We expect that, if a dynamic scenario applies when the most stable surface is considered, *a fortiori* less stable surfaces would exhibit a similar behaviour. A validation of this assertion can be found in Supplementary Figures 3-4, where we study how catalysis proceeds on the (001) surface.

In our simulation the (111) surface remains stable including the outermost layers (Fig. 1c,e and Supplementary Figure 5). Since at 750 K the catalyst is in the superionic phase, anions fluctuate around their equilibrium positions while cations diffuse rapidly (Supplementary Video 2). However, the behaviour of the surface changes dramatically when we let two ammonia molecules approach the surface so as to study the stochiometric reaction $2NH_3 \rightarrow N_2 + 3H_2$. On the time scale of nanoseconds the two ammonia molecules spontaneously react with two imides to give a total of four amides according to: $2NH^{2-} + 2NH_3 \rightarrow 4NH_2^-$ (Supplementary Video 3). This agrees with the experimental report that this is the first step in the cracking process[11]. As a consequence of this reaction two doubly charged NH^{2-} anions are transformed into four singly charged NH_2^- ones. After the reaction, the surface struggles to orderly accommodate the change in the number and charge of the anions and this leads to a novel dynamical behavior. Two amides move to the adlayer accompanied by some of the Li^+ while the two remaining amides replace two imides in the top layer (Fig. 1d,f and Supplementary Figure 5). Apart from short-lived fluctuations, this amide distribution is preserved during the simulation. From Figures 1d and Supplementary Figure 5 it clearly transpires that both amide and imide anions now exhibit a diffusive behaviour with the amides diffusing faster than the imide (Supplementary Videos 4 and 5), as to be expected given the larger charge of the latter. A quantitative description of these changes can be found in Supplementary Figure 6. In addition, on the time scale of nanoseconds protons can be spontaneously exchanged between amides and imides (Supplementary Figure 7 and Supplementary Video 6). Such Grotthus-like events have also been experimentally detected[11,14]. These changes are confined to the top two layers that now have a behavior akin to that of an ionic liquid. The present picture is consistent with the finding that non-stochiometric compounds like $Li_{2-x}(NH_2)_x(NH)_{1-x}$ have an increased activity[34,14]. In fact,

disorder, in particular charge disorder, will favor the formation of the activated dynamical state that is at the heart of this catalytic process.
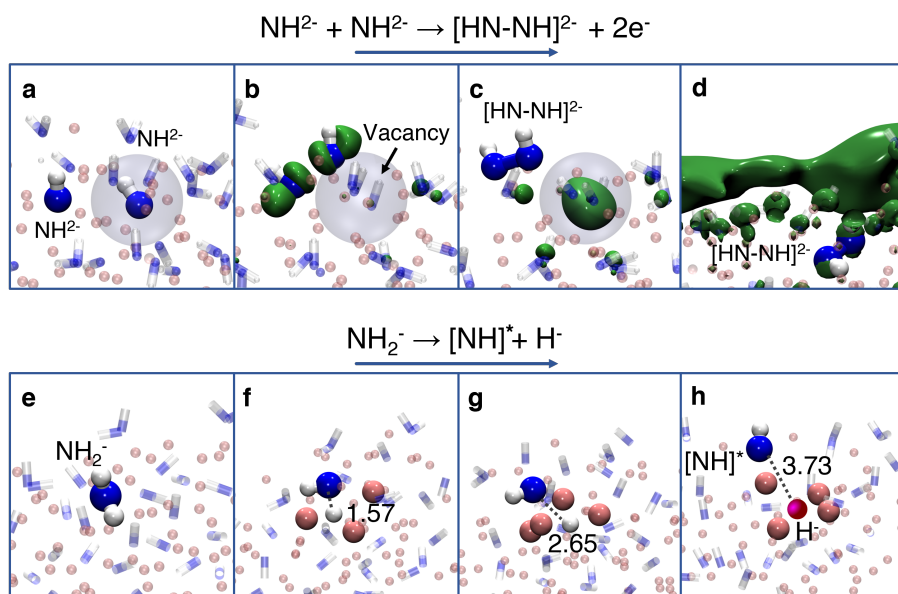
$$NH^{2-} + NH^{2-} \rightarrow [HN\text{-}NH]^{2-} + 2e^-$$

$$NH_2^- \rightarrow [NH]^* + H^-$$

Fig. 2 Schematic representation of the initial reaction steps. (**a-d**) Formation of the diazanediide anion ([HN-NH]$^{2-}$) as a result of the reaction: NH^{2-} + NH^{2-} → [HN-NH]$^{2-}$ + 2e^-. The position of one NH^{2-} before the reaction is marked with a grey transparent sphere (**a**). As the two NH^{2-} come close the [HN-NH]$^{2-}$ is formed and an ionic vacancy is left behind (**b**). The resulting cavity can localize the two electrons resulting from the [HN-NH]$^{2-}$ formation (**c**). These two electrons can also be accommodated in a diffuse surface state (**d**). In panels (**b-d**) the HOMO orbital is shown as a green solid isosurface. (**e-h**) Formation of the hydride (H$^-$) ion as a result of the reaction: NH$_2^-$ → [NH]* + H$^-$. An amide ion (**e**) is progressively stripped of one proton helped by the intervention of the Li$^+$ cations which stabilize the resulting H$^-$ (**f-h**). In panels (**f-h**) the N-H bond length (Å) is reported in black, and lithium atoms within 2.5 Å from the H atom are shown. Li, N, H and H$^-$ are coloured pink, blue, white, and purple, respectively.

The catalytic process

In this destabilized environment many reactions become possible. Discovering them all is extremely challenging and in a sense is beyond the scope of the present paper. To prove our point we only need to show that in the reactant induced scenario there are plausible pathways for ammonia decomposition.

Several likely reaction steps are reported in the Supplementary Note in a list that is far from exhaustive. All these steps have been discovered using our enhanced sampling method[30] (see Methods Section), and imposing that their free energy barriers are low enough for the reaction to take place at the *operando* temperature (Supplementary Table 1). Different steps can be concatenated in many different ways so as to eventually lead to the desired

products (Supplementary Figure 8). Of course the ability of the catalyst to allow different pathways increases its efficiency.

Here, we describe only two initial reaction steps that are paradigmatic of the way the activated ionic top layers catalyze reactions that would otherwise have been impossible. One of the initial steps leads to the formation of the diazanediide ($[\text{HN-NH}]^{2-}$) anion via the reaction $\text{NH}^{2-} + \text{NH}^{2-} \rightarrow [\text{HN-NH}]^{2-} + 2e^-$ (Fig. 2a-d and Supplementary Video 7). The highly fluxional ionic interlayer allows this reaction because the diazanediide is stabilized by a cloud of Li^+ cations (Supplementary Figure 9), and the two product electrons can be accommodated either in a diffuse surface state or in a state localized in an imide vacancy (Fig. 2c-d). These states are stabilized either by the Madelung energy or by the surface dipole.

One can liken this second localized state to that of a color centre in ionic crystals, a type of crystallographic defect in which an anionic vacancy is occupied by one or more electrons.[35, 36] Interestingly, recent experiments on ammonia decomposition on a CaNH-supported catalyst have suggested that color centres play a role also in this other catalytic process[37]. The solvated two electron state fluctuates from the diffuse to the localized variant (Supplementary Figure 10), and their nature is not affected by the inclusion of Hartree Fock exchange in the density functional (Supplementary Figure 11).
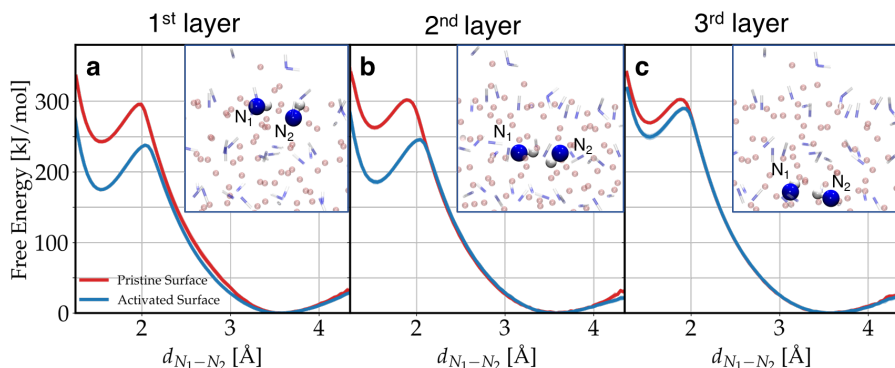

Fig. 3 Free energy surface for diazanediide formation. Three possible cases are reported in which the diazanediide anion is formed in the first (a), second (b) or third (c) layer. Free energy surfaces for the interlayer formation of the diazanediide are reported in Supplementary Figure 12. Results for the pristine and activated surfaces are reported in red and blue, respectively. The statistical errors are calculated using the weighted block-average technique as discussed in Ref. 38. Four blocks have been used, and errors are smaller than the linewidth. The two imide groups used to build the collective variable are reported in each panel. To simplify reading, a single instantaneous configuration is chosen to represent N and H atoms. Li, N and H atoms are coloured pink, blue, and white, respectively.

The free energy surface for diazanediide formation is reported in Fig. 3 for the pristine and activated surfaces. We compare three possible cases where the diazanediide anion is formed in the first (Fig. 3a), second (Fig. 3b) or third (Fig. 3c) layer, showing that the activated surface is more reactive than the

pristine one. Indeed, on the activated surface the reaction presents an activation barrier about 60 kJ/mol lower, and $[HN\text{-}NH]^{2-}$ is more stable because of the screening coming from the fluxional environment. Furthermore, the reaction is more likely to take place in the top two layers rather than in the innermost ones.

Another pathway to the formation of the diazanediide starts with the abstraction of a H^- from an amide. Such a reaction would have been impossible in the gas phase but here is made possible by the Li^+ intervention (Fig. 2**e-h** and Supplementary Video 8) that facilitates the breaking of the N-H bond, and the subsequent stabilization of H^-. An unusual polaronic intermediate state $[NH]^*$ is then formed. Analyzing the Bader charges[39] of this state we see that about two negative charges are associated to the [NH] while a compensating positive charge is distributed among the nitrogen atoms (Supplementary Figure 13). This $[NH]^*$ intermediate reacts with an imide leading to the formation of a diazanediide. Thus, the overall reaction can be read as NH_2^- + $NH^{2-} \rightarrow [HN\text{-}NH]^{2-}$ + H^-.

The three species $[HN\text{-}NH]^{2-}$, $2e^-$ and H^- then become the main actors in the reactions that follow. In one set of reactions the diazanediide is progressively stripped of its protons, eventually leading to the formation and release of an N_2 molecule (Fig. 4**a-c**).

The solvated $2e^-$ can abstract a proton from any of the nitrogen hydrides following the scheme $2e^- + NH_x^{(3\text{-x})\text{-}} \rightarrow NH_{x-1}^{(3\text{-}(x\text{-}1))\text{-}} + H^-$ (Fig. 4**d**). Finally, the presence of the H^- intermediate, that can be formed in many ways, is essential to the release of H_2 upon reaction with one nitrogen hydride molecule (Fig. 4**e-f**). By using the on-the-fly probability enhanced sampling flooding method[40], we characterized the kinetic rate of this step, computing a transition time τ of 9 ms (Supplementary Figure 14).

One of the possible catalytic cycles is resumed in Figure 5. Nevertheless, this is a simplified scheme, because we are in a situation in which the structure of the system changes continuously as the reaction proceeds, and there are multiple ways in which the reactive steps can take place and be concatenated before eventually leading to the products. The catalyst is a living system, and its working cannot be described as a result of a number of well-defined steps. A stochastic description of the reactive surface in such a fluctuating medium will have to be put in place.

Discussion

Overall, the decomposition of ammonia is a complex process that requires several steps, in which different metastable intermediates are formed. The catalytic activity of the destabilized surface results from its ability to store and give electrons and protons and of stabilizing negative intermediates. This is reminiscent of the way in which the enzyme nitrogenase works [41,42].

If we look at this process from a loftier standpoint we see that the highly dynamic behaviour induced by the first step in the ammonia decomposition
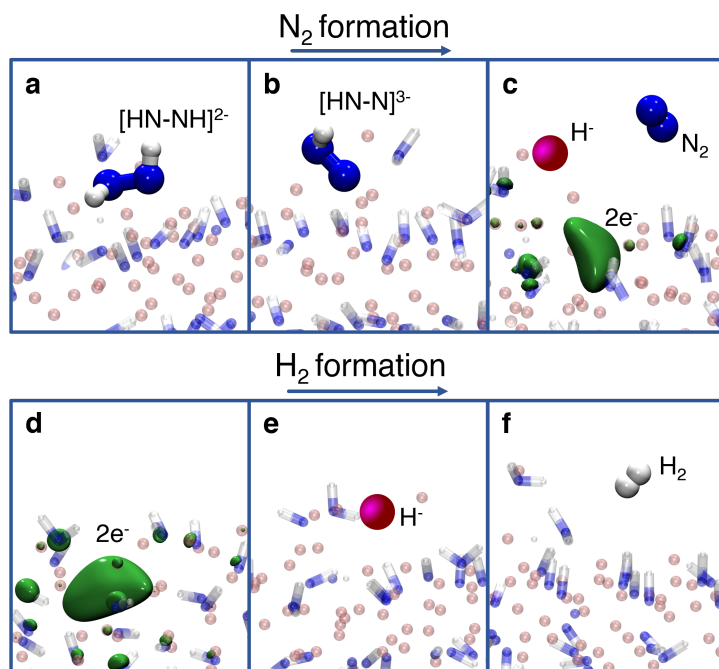
Fig. 4 Schematic of one representative set of decomposition reactions. The diazanediide anion (**a**) loses one proton forming diazanetriide [N-NH]$^{3-}$ (**b**) which can finally lead to N$_2$ (**c**). In addition, the solvated two electron state (**d**) can abstract a proton from the nitrogen hydrides species forming H$^-$ (**e**). The release of molecular hydrogen (**f**) from the hydride anion is then possible due to its strong basic character. In panels (**c-d**) the HOMO orbital is shown as a green solid isosurface. Li, N, H and H$^-$ are coloured pink, blue, white, and purple, respectively.

is what eventually leads to catalysis, and it is the surface and its subsurface volume that acts as a catalyst, instead of a specific atomic configuration. However, once started, the process is self sustained with the different reaction steps further contributing to the surface dynamical behaviour and therefore to its catalytic efficiency. Once the catalyst is no longer exposed to ammonia, the reaction stops, and the catalyst returns to its original state (Supplementary Figure 15). This system combines the benefit of a heterogeneous catalyst with a surface behavior similar to that of a homogeneous one. In our picture we do not deal with a catalysts that can have multiple metastable states[6, 7]. We have, in fact, discovered that during the reactions the interface undergoes a very dramatic change to a state that has properties different from those of the pristine surface.

There is other evidence that surface phase changes are relevant to heterogeneous catalysis. For instance, we have investigated the nitrogen activation on iron surfaces in *operando* conditions, and also in this case the catalytic activity is associated to a change in the physical state of the interface which
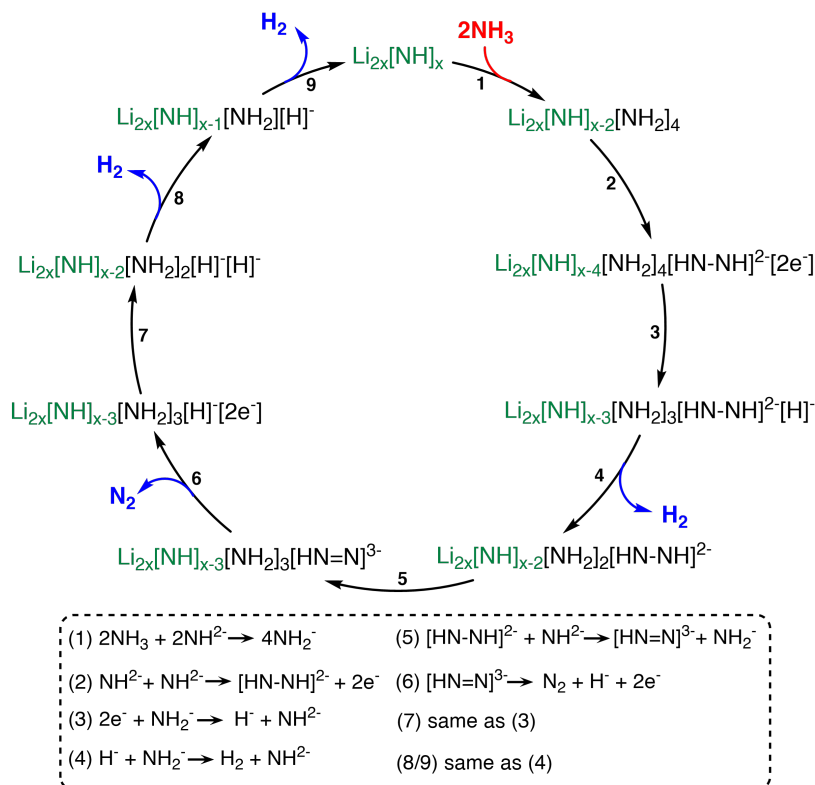
Fig. 5 Simplified scheme resuming the catalytic process. A list of all the observed reactions is reported in the SI, and other ways in which the different steps can be concatenated are shown in Supplementary Figure 8. The catalysis is highlighted in green, while reactants and products are shown in red and blue, respectively.

undergoes a global dynamical change, where the catalytic sites appear and disappear continuously[43]. This highly fluctuating environment is fundamental for the reaction to be sustained. Furthermore, the methane decomposition on copper surfaces must wait for copper to be close to the melting point in order to take place[44, 45]. Other evidence of a similar behaviour can be found in Ref.[4, 5]. We also note that often prior to production a catalyst has an induction period during which it undergoes dynamic changes[46, 47].

Conclusions

In conclusion, our study reveals that the flow of reactants modifies the dynamic behavior of the catalyst surface, resulting in a fluctuating interfacial state that acts as the catalytic medium. This finding challenges the conventional picture that a well-defined active site is solely responsible for the catalytic activity.

Our simulations reinforce Ertl's assertion in his Nobel address that a sampling approach is required to understand catalytic processes[48]. From our

simulations, it is clear that catalysis is a highly complex process. Only by taking complexity into consideration real progresses can be made. It is hoped that this insight will lead to the rational design of more efficient catalysts by appropriately engineering their interfacial behavior.

Methods

The superionic behaviour of Li_2NH was studied in a cubic supercell of edge 20.028 Å, containing 1024 atoms which amounts to replicate $2 \times 2 \times 2$ times the conventional unit cell[49] (Supplementary Figure 16**a**). The ammonia decomposition on the (111) surface was modeled using a slab made of 384 atoms in a monoclinic simulation box with edges $14.321, 14.321, 30.0$ Å, and $\gamma = 120°$ (Supplementary Figure 16**b**).

In this setup we left enough distance (about 15 Å) between replicas along the z direction to minimize interactions. In all the simulations of the (111) surface we fixed the atoms in the two bottom layers to their ideal crystal lattice positions to mimic the bulk environment.

We also studied the (001) surface with two possible terminations: Li^+ (Supplementary Figure 17**a**), and NH^{2-} (Supplementary Figure 17**b**). Since this is a charged surface care is required to set it up. To restore neutrality we followed the procedure described in Ref. 50, and moved half of the Li^+ or NH^{2-} ions from the outermost layer to the bottom one. Finally, we relaxed the whole structure. This led to a reconstruction of the top layer similar to what can be found in compounds like MgO[51]. This slab was made of 480 atoms in a tetragonal simulation cell with edges $15.95, 15.95, 30$ Å. This amounted to imposing a distance of about 15.0 Å between one slab and its periodic replicas in the z direction. During the molecular dynamics (MD) simulations we kept fixed the atoms in the bottom three layers.

We introduced two NH_3 molecules in the simulation box to study the ammonia decomposition reaction. To restraint the movement of the N atoms close to the surface, we limited d_z, the z component of the maximum distance between the N atoms and a ghost atom with xyz coordinates $0.0, 0.0, 15.0$ Å, to be smaller than $d_0 = 12$ Å. This is done by applying a harmonic restraint of the form $k/2(d_z\text{-}d_0)^2$ with $k/2 = 2000$ kJ/mol.

In the calculation of DFT energies and forces we used two different packages. *Ab initio* molecular dynamics (AIMD) simulations were performed using the Quickstep[52] module of the CP2K package[53] supplemented by the PLUMED 2.8 plugin[54], while the energies and forces needed for the Neural Network (NN) training were calculated using the PWSCF v.7.0 code from the Quantum Espresso package[55, 56, 57]. This latter was used to check the effect of the Brillouin zone k-points sampling. We satisfied ourselves that the use of Γ-point only was appropriate as expected. We checked that our NN can reproduce well also the CP2K forces. Furthermore, we used CP2K also to check the eigenfunctions with the HSE06 density functional[58].

We characterized the electronic states along the reaction pathways by computing eigenvalues, eigenfunctions and Bader charges[39] on representative configurations extracted from NN-based molecular dynamics. These calculations were performed using Quantum Espresso.

In the next sections all the simulation details are provided.

AIMD simulations

All the AIMD simulations were performed in the canonical ensemble (NVT) with periodic boundary conditions, and a time step of 0.5 fs. The temperature was controlled using the stochastic velocity rescaling thermostat[59] with a coupling constant of 0.05 ps. Energy and forces were computed using the Perdew–Burke–Ernzerhof (PBE) exchange-correlation functional[26]. The Kohn-Sham orbitals were expanded in a triple-ξ plus polarization (TZVP) Gaussian basis sets and the plane wave expansion of the electronic density was truncated at an energy cutoff of 300 Ry. The core electrons were treated using the Goedecker-Teter-Hutter (GTH) pseudopotentials[60,61] optimized for PBE. The AIMD simulations were performed on the (001) surface. This slab was made of 256 atoms in a tetragonal simulation cell[18] with edges $10.087, 10.087, 33$ Å.

Calculation of energies and forces

The DFT energies and forces needed for the NN training were calculated using again the PBE exchange-correlation functional. The RRKJUS PBE pseudopotential[62] taken from the QE pseudopotential library were used. The Kohn-Sham orbitals were expanded in plane waves basis set up to a kinetic-energy cutoff of 80 Ry and a density cutoff at 400 Ry. The convergence threshold for self-consistency was set to 1.0×10^{-7} a.u..

NN-based MD

The MD simulations that used the NN potential were performed by patching the DeepMD-kit software[63] implemented in LAMMPS[64] and PLUMED 2.8[54]. The canonical ensemble (NVT) was sampled in all the simulations, controlling the temperature with the stochastic velocity rescaling thermostat[59] with a coupling constant of 0.02 ps. A time step of 0.25 fs was used.

Enhanced sampling method: OPES

We used enhanced sampling simulations to explore the NH_3 decomposition reactions. Our strategy was based on enhancing the fluctuations of a set of carefully selected collective variables (CVs) $\boldsymbol{s}=\boldsymbol{s}(\boldsymbol{R})$ where $\boldsymbol{R}$ are the atomic coordinates. The CVs encoded the difficult to sample degrees of freedom of the system. We used the on-the-fly probability enhanced sampling (OPES) method to enhance the fluctuations of $\boldsymbol{s}$. In OPES, the equilibrium probability distribution $P(\boldsymbol{s})$ is first estimated on-the-fly, and then a bias potential $V_n(\boldsymbol{s})$ is constructed so as to converge the $\boldsymbol{s}$ distribution to a target one $P^{tg}(\boldsymbol{s})$.

Here, we used as target distribution the well-tempered one $P^{tg}(\boldsymbol{s}) \propto [P(\boldsymbol{s})]^{\frac{1}{\gamma}}$, where $\gamma > 1$ is the bias factor, and $\beta = 1/k_B T$. In this case, the bias

potential at n^{th} iteration is written as:

$$V_n(\boldsymbol{s}) = (1 - 1/\gamma)\frac{1}{\beta} \log\left(\frac{P_n(\boldsymbol{s})}{Z_n} + \epsilon\right) \tag{1}$$

where Z_n is a normalization factor, and $\epsilon = \mathrm{e}^{-\beta\Delta E/(1-1/\gamma)}$ is a regularization parameter that limits the maximum bias that can be deposited. This allows only the lowest free energy pathways to be explored avoiding the less likely higher energy reactions. The highest value of ΔE used was 200 kJ/mol. However, to generate the training configurations as described in the next section, we used larger values of ΔE (up to 300 kJ/mol) which allowed the generation of less likely configurations, thus increasing the robustness of the NN potential.

As in all the CV based enhanced sampling methods, also in OPES a good choice of the CVs is extremely important. When choosing the CVs, we tried as much as possible not to prejudge the outcome of the reaction, nor the identity of the atoms involved. A quantity that we found useful in the CV definition is the coordination number written as a continuous function in order to avoid discontinuities when calculating the forces coming from the bias:

$$C_{i\in A}^B = \sum_{j\in B}^{N_j} \frac{1 - (\frac{d_{ij}}{r_0})^n}{1 - (\frac{d_{ij}}{r_0})^m} \tag{2}$$

In the above equation, d_{ij} is the distance between atoms i and j, N_j is the number of atoms of species B, and the exponents n and m control the sharpness of the function. Here, we set $n = 6$ and $m = 12$. Thus, C_i^B measures how many atoms of species B are within a sphere of radius r_0 centred on atom i, and it allows forming or cleaving chemical bonds.

Depending on the circumstances, we use as CV the following combination of C_i^B:

$$S_{AB} = \sum_{i\in A} C_i^B \tag{3}$$

$$S_{AB}^{max} = \alpha \log \sum_{i\in A} \exp\left(\frac{C_i^B}{\alpha}\right) \tag{4}$$

$$S_{AB}^{min} = \frac{\beta}{\log \sum_{i\in A} \exp\left(\frac{C_i^B}{\beta}\right)} \tag{5}$$

S_{AB}^{max} and S_{AB}^{min} are soft max and soft min functions that select the atoms with the highest and lowest coordination number, respectively.

We used a sequential strategy to discover the set of reactions that led to N_2 and H_2. After a novel reaction step was discovered, we took the newly discovered species and applied the CV that was most appropriate for the reaction to proceed. In Table S1 we list the CVs and biases ΔE used, together with the products that these CVs have helped discovering. These CVs were used in both the NN training and production simulations.

NN training

The NN potentials were trained using the Deep Potential-Smooth Edition scheme[65] as implemented in the DeePMD-kit package[63]. This model consists of two neural networks: the embedding and the fitting one. Both networks use the ResNet architecture. We chose an embedding network with three hidden layers and $(30, 60, 120)$ nodes/layer. The size of the embedding matrix has been set to 16. Four hidden layers with $(240, 240, 240, 240)$ nodes/layer were used in the fitting network. The cutoff radius was set to 8.0 Å and the descriptors decay smoothly from 0.5 Å to 8.0 Å. The learning rate decays from 1.0×10^{-3} to 5.0×10^{-8}. The batch size was set to 8. The following loss function was minimized during training:

$$L(\alpha_E, \alpha_f, \alpha_\xi) = \alpha_E \, \Delta E^2 + \frac{\alpha_f}{3N} \sum_i \Delta \boldsymbol{F}_i^2 + \frac{\alpha_\xi}{9} \|\Delta \xi\|^2 \qquad (6)$$

where $\alpha_E, \alpha_f, \alpha_\xi$ are the energy force and the virial tensor prefactors, respectively. Δ denotes the difference between the DeePMD prediction of the energy, forces and virial and the training data, N is the number of atoms, E is the energy per atom, $\boldsymbol{F}_i$ is the force on atom i, and ξ is the virial tensor$= -\frac{1}{2} \sum_i \boldsymbol{R}_i \otimes \boldsymbol{F}_i$. The prefactors of the energy and force terms in the loss function changed from 0.05 to 5 and from 1000 to 1, respectively. The virial term was also included in the loss function with prefactor value changing from 0.01 to 1. In the initial training phase 1.0×10^6 training steps were used. In order to obtain the final NN model this number was doubled.

Setting up the training set

The construction of the NN potential for such a multi-component reactive system is the most challenging part of the work, and requires a careful balance between computational effort and sufficient coverage of the configuration space. In our case, this is made harder by the fact that we have to model a highly reactive system, and therefore many rare but critical events need to be explored, and the potential energy for these events accurately predicted.

An active learning approach assisted by the enhanced sampling method OPES[30, 38] was used to explore the relevant configurations involved in the NH_3 decomposition process (Supplementary Figure 18). This strategy has already been successfully applied to study several other complex systems[31, 27, 29, 28].

First, we used about 3900 atomic configurations from the AIMD simulations performed on the smaller 256 atoms system described above representing the (001) surface, and built an initial training set. About 70 short AIMD simulations ranging from 1 to 6 ps were performed at the temperatures of 600 K, 700 K, and 750 K.

As the NN potential building proceeded we added configurations taken from the (111) surface. Our active learning procedure made sure that we considered reactive configurations.

The OPES method has been adopted to enhance the exploration of possible

reactive configurations and reaction pathways. Starting from these configurations and the associated DFT energies and forces, we have followed an active learning approach (Supplementary Figure 18) to extend and refine the training set. Each active learning iteration involved the following steps:

Step 1: Four NN potentials using different initial weights were trained based on the same training set as the previous iteration;

Step 2: A series of NN-based OPES simulations were performed to explore new relevant atomic configurations and reaction pathways. We computed for each configuration a local estimate of the reliability of the NN. This was measured by σ[66], defined as the maximal standard deviation of the atomic forces predicted by these four NN potentials:

$$\sigma = \max_{i} \sqrt{\frac{1}{4} \sum_{\alpha=1}^{4} \| \boldsymbol{F}_i^{\alpha} - \overline{\boldsymbol{F}_i} \|^2} \tag{7}$$

where $\boldsymbol{F}_i^{\alpha}$ is the atomic force on the atom i predicted by the NN potential α, and $\overline{\boldsymbol{F}_i}$ is the average force on the atom i over the four NN potentials.

Similarly to what was done in Ref. 29, 28 we have set up an empirical strategy to minimize the number of new DFT calculations. For this reason, we set a lower bound (σ_l) to the error σ and an upper limit (σ_u) which is usually associated with nonphysical configurations in which atoms are too close or correspond to improbable chemistry. In detail, σ_l was set to a value slightly higher than the average model deviation of the latest training set, while the choice of the σ_u was based on the rule ($[0.20 \sim 0.30 \text{ ev/Å}] + \sigma_l$). The configurations with $\sigma > \sigma_u$ were outright rejected; the rest is divided into four intervals defined as follows (Supplementary Figure 19):

a) $0 < \sigma \leq \sigma_l - 0.05$
b) $\sigma_l - 0.05 < \sigma \leq \sigma_l$
c) $\sigma_l < \sigma \leq \sigma_l + 0.10$
d) $\sigma_l + 0.10 < \sigma \leq \sigma_u$

The intervals c and d are larger because the distribution of errors has a long tail. The configurations in a were automatically included among those that are described well by the NN model at this stage of the training. In the bins b, c, and d there will be N_b, N_c, and N_d configurations and for these intervals we selected a fraction of configurations with percentages in the ratio $\sim 1 : 5 : 20$. The absolute values of these numbers were chosen to control the number of DFT calculations needed. Our rule favors selecting configurations in the c and d intervals that are most instrumental in expanding the variety of configurations added to the training data set. After this first iteration, a new NN was trained using the expanded data set. The error σ associated with this NN was computed and used as σ for the new iteration.

Step 3: The DFT energies and forces of the configurations selected in step 2 were added to the training data set and the NN was retrained.

Following our previous work[29], we updated the training set until the percentage of configurations in intervals c and d reached $\sim 10 \%$ and remained

almost unchanged for a few other iterations. In the end, a total of $\sim 10^5$ atomic configurations were used.

Validation of the NN model

The mean absolute errors (MAEs) of energies in the training and test set are 0.85 meV/atom and 0.90 meV/atom, respectively. The MAEs of forces in the training and test set are 37.59 meV/Å and 38.04 meV/Å, respectively. The test set consisted of ~ 5700 configurations collected from the transition state regions of the reactions sampled in the NN-based OPES simulation at 750 K. We included in the test set configurations corresponding to the intermediates and transitions states of all the steps discussed in the main text. The comparison of DFT and the corresponding NN predicted atomic energies and forces over the test sets is given in Fig. S5**a**. Furthermore, we analysed the MAEs for two fundamental reaction steps: ammonia reaction on the (111) surface, and N-N bond formation (Supplementary Figure 20**B**,**C**).

Data availability. All the inputs and instructions to reproduce the results presented in this manuscript can be found in the PLUMED-NEST repository.

Author contributions Statement. M.Y., U.R., and M.P. made substantial contributions to the design and implementation of the work and wrote the manuscript.

Competing Interests Statement. The authors declare no competing interests.

References

[1] Lucentini, I., Garcia, X., Vendrell, X. & Llorca, J. Review of the decomposition of ammonia to generate hydrogen. *Ind. Eng. Chem. Res.* **60**, 18560–18611 (2021) .

[2] Friend, C. M. & Xu, B. Heterogeneous catalysis: a central science for a sustainable future. *Acc. Chem. Res.* **50**, 517–521 (2017) .

[3] Schlögl, R. Heterogeneous catalysis. *Angew. Chem., Int. Ed.* **54**, 3465–3520 (2015) .

[4] Spencer, M. Stable and metastable metal surfaces in heterogeneous catalysis. *Nature* **323**, 685–687 (1986) .

[5] Topsøe, H. Developments in operando studies and in situ characterization of heterogeneous catalysts. *J. Catal.* **216**, 155–164 (2003) .

[6] Zhang, Z., Zandkarimi, B. & Alexandrova, A. N. Ensembles of metastable states govern heterogeneous catalysis on dynamic interfaces. *Acc. Chem. Res.* **53**, 447–458 (2020) .

[7] Sun, G. & Sautet, P. Active site fluxional restructuring as a new paradigm in triggering reaction activity for nanocluster catalysis. *Acc. Chem. Res.* **54**, 3841–3849 (2021) .

[8] Wang, Y.-G., Mei, D., Glezakou, V.-A., Li, J. & Rousseau, R. Dynamic formation of single-atom catalytic active sites on ceria-supported gold nanoparticles. *Nat. Commun.* **6**, 1–8 (2015) .

[9] Chen, P., Xiong, Z., Luo, J., Lin, J. & Tan, K. L. Interaction of hydrogen with metal nitrides and imides. *Nature* **420**, 302–304 (2002) .

[10] David, W. I. F. *et al.* A mechanism for non-stoichiometry in the lithium amide/lithium imide hydrogen storage reaction. *J. Am. Chem. Soc.* **129**, 1594–1601 (2007). PMID: 17243680 .

[11] Makepeace, J. W., Wood, T. J., Hunter, H. M. A., Jones, M. O. & David, W. I. F. Ammonia decomposition catalysis using non-stoichiometric lithium imide. *Chem. Sci.* **6**, 3805–3815 (2015) .

[12] Guo, J. *et al.* Lithium imide synergy with 3d transition-metal nitrides leading to unprecedented catalytic activities for ammonia decomposition. *Angew. Chem., Int. Ed.* **54**, 2950–2954 (2015) .

[13] Mukherjee, S., Devaguptapu, S. V., Sviripa, A., Lund, C. R. & Wu, G. Low-temperature ammonia decomposition catalysts for hydrogen generation. *Appl. Catal., B* **226**, 162–181 (2018) .

[14] Makepeace, J. W. *et al.* Compositional flexibility in Li-N-H materials: implications for ammonia catalysis and hydrogen storage. *Phys. Chem. Chem. Phys.* **23**, 15091–15100 (2021) .

[15] Car, R. & Parrinello, M. Unified approach for molecular dynamics and density-functional theory. *Phys. Rev. Lett.* **55**, 2471 (1985) .

[16] Juza, R. & Opp, K. Metallamide und metallnitride, 25. mitteilung. zur kenntnis des lithiumimides. *Z. anorg. allg. Chem.* **266**, 325–330 (1951) .

[17] Noritake, T. *et al.* Crystal structure and charge density analysis of Li_2NH by synchrotron X-ray diffraction. *J. Alloys Compd.* **393**, 264–268 (2005) .

[18] Balogh, M. P., Jones, C. Y., Herbst, J., Hector Jr, L. G. & Kundrat, M. Crystal structures and phase transformation of deuterated lithium imide, Li_2ND. *J. Alloys Compd.* **420**, 326–336 (2006) .

[19] Miceli, G., Ceriotti, M., Bernasconi, M. & Parrinello, M. Static disorder and structural correlations in the low-temperature phase of lithium imide. *Phys. Rev. B* **83**, 054119 (2011) .

[20] Hull, S. Superionics: crystal structures and conduction processes. *Rep. Prog. Phys.* **67**, 1233–1314 (2004) .

[21] Araújo, C. M., Blomqvist, A., Scheicher, R. H., Chen, P. & Ahuja, R. Superionicity in the hydrogen storage material Li_2NH: Molecular dynamics simulations. *Phys. Rev. B* **79**, 172101 (2009) .

[22] Miceli, G., Ceriotti, M., Angioletti-Uberti, S., Bernasconi, M. & Parrinello, M. First-principles study of the high-temperature phase of Li_2NH. *J. Phys. Chem. C* **115**, 7076–7080 (2011) .

[23] Behler, J. & Parrinello, M. Generalized neural-network representation of high-dimensional potential-energy surfaces. *Phys. Rev. Lett.* **98**, 146401 (2007) .

[24] Zhang, L., Han, J., Wang, H., Car, R. & Weinan, E. Deep potential molecular dynamics: a scalable model with the accuracy of quantum mechanics. *Phys. Rev. Lett.* **120**, 143001 (2018) .

[25] Parr, R. G. *Density functional theory of atoms and molecules* (Springer, 1980).

[26] Perdew, J. P., Burke, K. & Ernzerhof, M. Generalized gradient approximation made simple. *Phys. Rev. Lett.* **77**, 3865 (1996) .

[27] Niu, H., Bonati, L., Piaggi, P. M. & Parrinello, M. *Ab initio* phase diagram and nucleation of gallium. *Nat. Commun.* **11**, 1–9 (2020) .

[28] Yang, M., Bonati, L., Polino, D. & Parrinello, M. Using metadynamics to build neural network potentials for reactive events: the case of urea decomposition in water. *Catal. Today* **387**, 143–149 (2022) .

[29] Yang, M., Karmakar, T. & Parrinello, M. Liquid-liquid critical point in phosphorus. *Phys. Rev. Lett.* **127**, 080603 (2021) .

[30] Invernizzi, M. & Parrinello, M. Rethinking metadynamics: from bias potentials to probability distributions. *J. Phys. Chem. Lett.* **11**, 2731–2736 (2020) .

[31] Bonati, L. & Parrinello, M. Silicon liquid structure and crystal nucleation from *ab initio* deep metadynamics. *Phys. Rev. Lett.* **121**, 265701 (2018) .

[32] Gartner III, T. E., Piaggi, P. M., Car, R., Panagiotopoulos, A. Z. & Debenedetti, P. G. Liquid-liquid transition in water from first principles. *Phys. Rev. Lett.* **129**, 255702 (2022) .

[33] Meuwly, M. Machine learning for chemical reactions. *Chem. Rev.* **121**, 10218–10239 (2021) .

[34] Makepeace, J. W., Jones, M. O., Callear, S. K., Edwards, P. P. & David, W. I. F. In situ X-ray powder diffraction studies of hydrogen storage and release in the Li–N–H system. *Phys. Chem. Chem. Phys.* **16**, 4061–4070 (2014) .

[35] Seitz, F. Color centers in alkali halide crystals. *Rev. Mod. Phys.* **18**, 384 (1946) .

[36] Crawford, J. H. & Slifkin, L. M. *Point Defects in Solids: General and ionic crystals* (Springer Science, 1972).

[37] Ogasawara, K. *et al.* Ammonia decomposition over CaNH-Supported Ni catalysts via an NH_2-vacancy-mediated Mars-van krevelen mechanism. *ACS Catal.* **11**, 11005–11015 (2021) .

[38] Invernizzi, M., Piaggi, P. M. & Parrinello, M. Unified approach to enhanced sampling. *Phys. Rev. X.* **10**, 041034 (2020) .

[39] Henkelman, G., Arnaldsson, A. & Jónsson, H. A fast and robust algorithm for bader decomposition of charge density. *Comput. Mater. Sci.* **36**, 354–360 (2006) .

[40] Ray, D., Ansari, N., Rizzi, V., Invernizzi, M. & Parrinello, M. Rare event kinetics from adaptive bias enhanced sampling. *J. Chem. Theory Comput.* **18**, 6500–6509 (2022) .

[41] Hoffman, B. M., Lukoyanov, D., Dean, D. R. & Seefeldt, L. C. Nitrogenase: a draft mechanism. *Acc. Chem. Res.* **46**, 587–595 (2013) .

[42] Seefeldt, L. C. *et al.* Energy transduction in nitrogenase. *Acc. Chem. Res.* **51**, 2179–2186 (2018) .

[43] Bonati, L. *et al.* Non-linear temperature dependence of nitrogen adsorption and decomposition on fe (111) surface. *ChemRxiv. Cambridge: Cambridge Open Engage* (2023) .

[44] Li, P., Zeng, X. & Li, Z. Understanding high-temperature chemical reactions on metal surfaces: A case study on equilibrium concentration and diffusivity of c x h y on a cu (111) surface. *JACS Au* **2**, 443–452 (2022) .

[45] Gao, H. *et al.* Graphene at liquid copper catalysts: atomic-scale agreement of experimental and first-principles adsorption height. *Adv. Sci.* **9**, 2204684 (2022) .

[46] Hansen, P. L. *et al.* Atom-resolved imaging of dynamic shape changes in supported copper nanocrystals. *Science* **295**, 2053–2055 (2002) .

[47] Xu, L. *et al.* Formation of active sites on transition metals through reaction-driven migration of surface atoms. *Science* **380**, 70–76 (2023) .

[48] Ertl, G. Reactions at surfaces: from atoms to complexity (Nobel lecture). *Angew. Chem., Int. Ed.* **47**, 3524–3535 (2008) .

[49] Bonnet, M.-L., Iannuzzi, M., Sebastiani, D. & Hutter, J. Local disorder in lithium imide from density functional simulation and NMR spectroscopy. *J. Phys. Chem. C* **116**, 18577–18583 (2012) .

[50] Miceli, G., Cucinotta, C. S., Bernasconi, M. & Parrinello, M. First principles study of the $LiNH_2/Li_2NH$ transformation. *J. Phys. Chem. C* **114**, 15174–15183 (2010) .

[51] Tasker, P., Colbourn, E. & Mackrodt, W. Segregation of isovalent impurity cations at the surfaces of MgO and CaO. *J. Am. Ceram. Soc.* **68**, 74–80 (1985) .

[52] VandeVondele, J. *et al.* Quickstep: Fast and accurate density functional calculations using a mixed gaussian and plane waves approach. *Comput. Phys. Commun.* **167**, 103–128 (2005) .

[53] Maintz, S., Deringer, V. L., Tchougréeff, A. L. & Dronskowski, R. Lobster: A tool to extract chemical bonding from plane-wave based DFT (2016).

[54] Tribello, G. A., Bonomi, M., Branduardi, D., Camilloni, C. & Bussi, G. PLUMED 2: New feathers for an old bird. *Comput. Phys. Commun.* **185**, 604–613 (2014) .

[55] Giannozzi, P. *et al.* QUANTUM ESPRESSO: a modular and open-source software project for quantum simulations of materials. *J. Phys.: Condens. Matter* **21**, 395502 (2009) .

[56] Giannozzi, P. *et al.* Advanced capabilities for materials modelling with Quantum ESPRESSO. *J. Phys.: Condens. Matter* **29**, 465901 (2017) .

[57] Giannozzi, P. *et al.* Quantum espresso toward the exascale. *J. Chem. Phys.* **152**, 154105 (2020) .

[58] Krukau, A. V., Vydrov, O. A., Izmaylov, A. F. & Scuseria, G. E. Influence of the exchange screening parameter on the performance of screened hybrid functionals. *J. Chem. Phys.* **125**, 224106 (2006) .

[59] Bussi, G., Donadio, D. & Parrinello, M. Canonical sampling through velocity rescaling. *J. Chem. Phys.* **126**, 014101 (2007) .

[60] Goedecker, S., Teter, M. & Hutter, J. Separable dual-space gaussian pseudopotentials. *Phys. Rev. B* **54**, 1703 (1996) .

[61] Hartwigsen, C., Gœdecker, S. & Hutter, J. Relativistic separable dual-space gaussian pseudopotentials from h to rn. *Phys. Rev. B* **58**, 3641 (1998) .

[62] Rappe, A. M., Rabe, K. M., Kaxiras, E. & Joannopoulos, J. Optimized pseudopotentials. *Phys. Rev. B* **41**, 1227 (1990) .

[63] Wang, H., Zhang, L., Han, J. & Weinan, E. DeePMD-kit: A deep learning package for many-body potential energy representation and molecular dynamics. *Comput. Phys. Commun.* **228**, 178–184 (2018) .

[64] Thompson, A. P. *et al.* LAMMPS-a flexible simulation tool for particle-based materials modeling at the atomic, meso, and continuum scales. *Comput. Phys. Commun.* **271**, 108171 (2022) .

[65] Zhang, L. *et al.* End-to-end symmetry preserving inter-atomic potential energy model for finite and extended systems. *Adv. Neural Inf. Process.* **31** (2018) .

[66] Zhang, Y. *et al.* DP-GEN: A concurrent learning platform for the generation of reliable deep learning based potential energy models. *Comput. Phys. Commun.* **253**, 107206 (2020) .